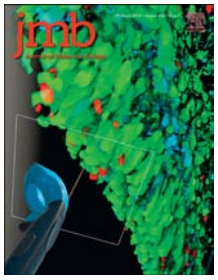

Cryo-EM Structures Reveal Relocalization of MetAP in the Presence of Other Protein Biogenesis Factors at the Ribosomal Tunnel Exit

Sayan Bhakta[†], **Shirin Akbar**[†] **and Jayati Sengupta**

Structural Biology & Bio-Informatics Division, *CSIR-Indian Institute of Chemical Biology, 4, Raja S.C. Mullick Road, Kolkata 700 032, India*

Correspondence to Jayati Sengupta: *jayati@iicb.res.in*
https://doi.org/10.1016/j.jmb.2019.02.002
Edited by E. Nogales

Abstract

During protein biosynthesis in bacteria, one of the earliest events that a nascent polypeptide chain goes through is the co-translational enzymatic processing. The event includes two enzymatic pathways: deformylation of the N-terminal methionine by the enzyme peptide deformylase (PDF), followed by methionine excision catalyzed by methionine aminopeptidase (MetAP). During the enzymatic processing, the emerging nascent protein likely remains shielded by the ribosome-associated chaperone trigger factor. The ribosome tunnel exit serves as a stage for recruiting proteins involved in maturation processes of the nascent chain. Co-translational processing of nascent chains is a critical step for subsequent folding and functioning of mature proteins.

Here, we present cryo-electron microscopy structures of *Escherichia coli* (*E. coli*) ribosome in complex with the nascent chain processing proteins. The structures reveal overlapping binding sites for PDF and MetAP when they bind individually at the tunnel exit site, where L22–L32 protein region provides primary anchoring sites for both proteins. In the absence of PDF, trigger factor can access ribosomal tunnel exit when MetAP occupies its primary binding site. Interestingly, however, in the presence of PDF, when MetAP's primary binding site is already engaged, MetAP has a remarkable ability to occupy an alternative binding site adjacent to PDF. Our study, thus, discloses an unexpected mechanism that MetAP adopts for context-specific ribosome association.

Introduction

Ribosome not only serves as a platform for protein biosynthesis but also plays a crucial role in regulating various co-translational maturation steps related to protein biogenesis, including N-terminal enzymatic processing of the nascent chain [1,2]. Emergence from the ribosome exit tunnel marks the onset of the maturation processes of the nascent polypeptide chain. The tunnel exit of the *Escherichia coli* 50S subunit is surrounded by ribosomal proteins (L17, L22, L23, L24, L29, and L32) along with 23S rRNA helices (domains I and III) [3,4]. These proteins and rRNA domains around the tunnel exit serve as docking sites for co-translational enzymes and chaperones [4].

In eubacteria, the nascent polypeptide chain encounters multiple members of a large repertoire of protein factors, which primarily includes peptide deformylase (PDF), methionine aminopeptidase (MetAP/MAP), trigger factor (TF), signal recognition particle (SRP), and SecYEG translocon [1]. Structural studies have demonstrated that SRP, TF, and SecYEG share overlapping binding sites on the ribosome [5–8], suggesting that the same platform is used for multiple functions. How the proteins modulate their anchoring positions on ribosome and accommodate one another in order to access the nascent chain properly is an interesting and yet unexplained question.

Protein synthesis in bacteria is initiated with N-formyl methionine [9,10]. As soon as the newly synthesized polypeptide chain reaches the extremity of the ribosomal exit tunnel, it first encounters PDF protein (essential in bacteria), which removes the N-terminal formyl group (deformylation) [9]. PDF, a metalloenzyme, utilizes Fe (II) as the catalytic metal ion, which can be replaced with nickel or cobalt ion with no loss of activity [11,12]. Depending on structure and sequence similarity, PDFs are classified into three types (1, 2, and 3) [10]. PDF in *E. coli* belongs to subtype 1b [13].

Deformylation is a prerequisite for subsequent N-terminal methionine excision needed to produce diverse N termini in proteins for their appropriate function, targeting and eventual degradation. MetAP, which is present in all kingdoms of life [14], is an enzyme that catalyzes the cleavage of first methionine from the growing polypeptide chain containing small and uncharged penultimate residue [15]. MetAPs also encompass metal binding site and can be activated by various divalent metal cations, but unlike PDFs, the physiological metal ions of MetAPs are still a matter of debate [16]. Sequence and structural characterizations have identified two types of MetAPs, MetAP1 and MetAP2. *E. coli* has MetAP subtype1a, comprising only the catalytic domain, while eukaryotes possess both classes [10,17–20].

The coordination and dynamics of several tunnel-associated, protein targeting factors (e.g., SRP and the translocon) have been investigated structurally in great detail [21–25]. However, only limited structural and functional studies related to the nascent chain processing enzymes in *E. coli* system have been reported so far [1,10,26]. It has been established that the C-terminal helical extension of *E. coli* PDF is responsible for ribosome association. A crystal structure of the C-terminal helix of PDF in complex with the 70S ribosome has provided a model for PDF binding on the ribosome [13]. The structure showed the ribosome-interacting C-terminal helix binding to a groove between ribosomal proteins L22 and L32, placing its active site towards the tunnel exit, thereby providing easy access for the emerging nascent polypeptides to interact with. The ribosome interaction site of the MetAP, however, has not been clearly identified thus far, although several lines of evidence suggest that there is an association between MetAP and ribosome at the exit site of the ribosome tunnel [26]. Biochemical and rigorous modeling studies have indicated the surface between L23 and L17 as MetAP interaction site, where a positively charged loop of MetAP is the putative ribosome binding motif [27]. Structural and functional studies have demonstrated that TF, the only ribosome-associated chaperone in bacteria, adopts a cradle-shape where its N-terminal domain binds to L23 protein at the tunnel exit, whereas the other domains [peptidylprolyl isomerise (PPIase) and C-terminal "arms"] project over the exit of the ribosomal tunnel [1,28–33] to protect the emerging nascent polypeptide chain. It is evident that despite some progress, our understanding on how the tunnel-binding factors interact with one another while simultaneously accessing the site remains insufficient.

In this study, we present a structural overview of the interactions of the nascent chain processing factors with the *E. coli* 70S ribosome. Since the presence of nascent polypeptide chain in the peptide tunnel is not a prerequisite for binding of the ribosome-associated, co-translational nascent chain processing factors [13,27], we have used purified *E. coli* 70S ribosomes to make the ribosomal complexes. By means of cryo-electron microscopy (cryo-EM) and three-dimensional (3D) single-particle reconstruction techniques, five maps (~10 to 15Å resolution range) have been generated. Three of these demonstrate binding of the nascent chain processing enzymes (PDF, MetAP) to 70S ribosome either individually (70S–PDF and 70S–MetAP complexes) or together (70S–PDF–MetAP complex). The other two maps represent interaction of ribosome with chaperone TF in the presence of PDF and/or MetAP (70S–MetAP–TF and 70S–PDF–TF complexes). The cryo-EM maps revealed overlapping binding sites of PDF and MetAP near the tunnel exit (at L22–L32 protein region), when allowed to associate with the ribosome individually (70S–PDF and 70S–MetAP complexes). Structure of the 70S ribosome in complex with MetAP and TF further confirmed the L22–L32 protein region as the primary binding site of MetAP. In contrast, when MetAP interacts with the 70S–PDF pre-complex, it relocates to a neighboring site close to L23 (secondary binding site), whereas PDF stays at the same L22–L32 region (70S–PDF–MetAP complex). Interestingly, eukaryotic MetAP2 homolog Arx1 protein binding site on ribosome [34–36] overlaps with the secondary binding site of MetAP in this complex. Another cryo-EM structure revealed the interaction of TF with the 70S ribosome pre-complexed with PDF and MetAP (70S–PDF–MetAP complex). Although clear densities corresponding to PDF and TF were seen in this map, confirming that these two proteins can access ribosome simultaneously [37], no obvious density corresponding to MetAP was found. We termed this complex as 70S–PDF–TF complex. It was not possible to simultaneously visualize PDF, TF, and MetAP bound to the ribosome in this complex, possibly because the N-terminal domain of TF overlaps considerably with MetAP in its secondary position (as seen in 70S–PDF–MetAP complex).

Taken together, our results reveal remarkable dynamic interplay of the protein biogenesis factors on the tunnel exit of the ribosome during co-translational processing of the nascent polypeptide chain.

Results

PDF binding to the *E. coli* 70S ribosome tunnel exit

Purified *E. coli* 70S ribosomes were used to make the complex with *E. coli* PDF following co-sedimentation procedure (Fig. S1d, e). A 3D cryo-EM map was generated for the PDF-bound 70S ribosome complex (map I, 70S–PDF complex, Fig. 1a). Additional density attributable to the PDF protein was visible at the tunnel exit site in the 3D map (Fig. 1a).

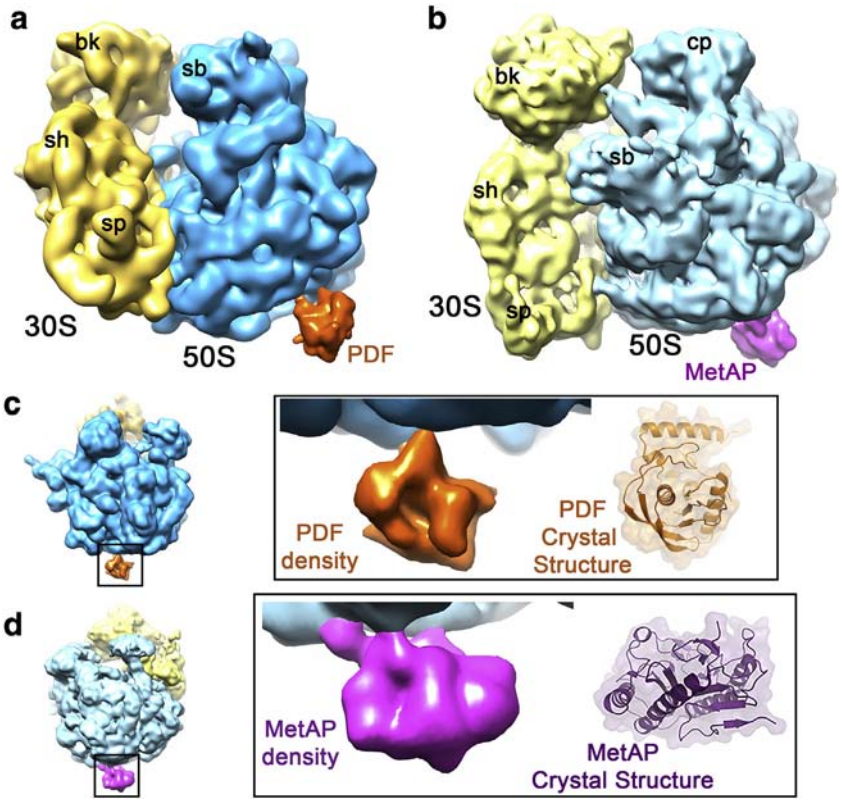

Fig. 1. Visualization of PDF and MetAP at the ribosome tunnel exit when bound individually. (a) Cryo-EM reconstruction of *E. coli* 70S ribosome–PDF complex showing the ligand at the tunnel exit site. The 30S subunit is shown in yellow, 50S subunit in blue, and the additional density for PDF in orange. (b) Cryo-EM reconstruction of *E. coli* 70S ribosome–MetAP complex. Density for MetAP is shown in magenta. Close-up views of PDF (c) and MetAP (d) densities show overall shape similarities to the crystal structures of respective proteins. Since the occupancies of the ligands were low in these maps (when PDF/MetAP binds singly), isolated ligand densities are shown here in lower contour levels. Landmarks for the 30S subunit: bk, beak; sh, shoulder; sp., spur. Landmarks for the 50S subunit: CP, central protuberance; sb, L7/L12 stalk base.

The presence of PDF density at the tunnel exit was also visible in some of the views of the two-dimensional class averages (Fig. S2a). Although ligand occupancy was low in this complex, the PDF density appeared to be very similar to the overall shape and size of the crystal structures [38] (Figs. 1c and S3a). We have generated the atomic model of the 70S–PDF complex using molecular dynamics flexible fitting (MDFF) approach (Fig. S3c). During MDFF simulation, we first performed flexible fitting of the rRNA coordinates. The RNA part was then kept rigid, while the tunnel-bound r-proteins were fitted. Finally, the rRNA and protein coordinates were kept rigid, and the ligand coordinate was fitted into the density map as a rigid body. The crystal structure of the ribosome-binding C-terminal helix of *E. coli* PDF in complex with the 70S ribosome depicted the position and interactions of the helix near the tunnel exit [13]. Localization of the C-terminal helix of PDF was done using this reported structure (PDB: 4V5B). Following fitting, the C-terminal ribosome-binding helix of PDF was found to be accommodated in a groove created between large subunit proteins L22 and L32, adjacent to nascent polypeptide tunnel exit (Fig. 2b). The fitted PDF structure was in overall agreement with previous finding [13]. A closer look at the PDF-binding region of the atomic model identified the involvement of rRNA as well as proteins around the tunnel exit in the interactions with PDF (Fig. 2b). The C-terminal helix is accommodated in the groove made by the 23S rRNA helices H24 (domain I) and H47 (domain III) and interacts with protein L22 (Fig. 2b). However, at current resolution of the map, the helix density remained fused with the 50S subunit density, thus limiting any further analysis.

MetAP binds to an overlapping region of PDF binding site

Similar co-sedimentation approach was taken to make MetAP-bound *E. coli* 70S ribosome complex (map II, 70S–MetAP complex, Fig. S1c). The 3D cryo-EM map (70S–MetAP, Fig. S2b) showed the presence of an extra ribosomal density near the

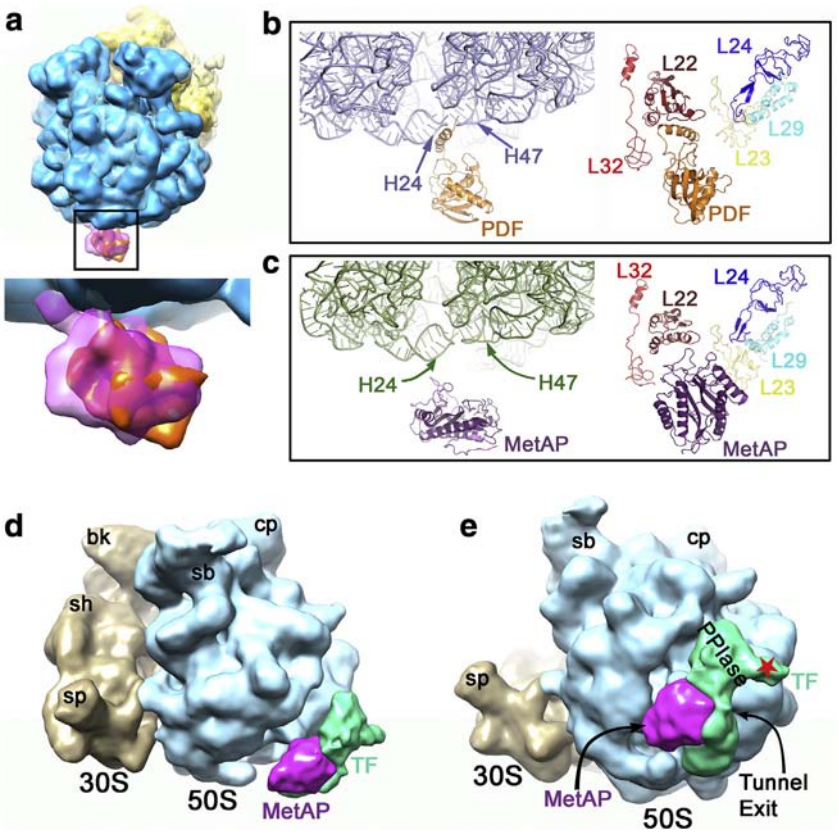

Fig. 2. Quasi-atomic models for 70S–PDF and 70S–MetAP complexes and cryo-EM reconstruction of 70S–MetAP–TF complex. (a) Superposition of the cryo-EM maps of 70S–PDF and 70S MetAP complexes shows overlapping binding sites of PDF (solid, orange) and MetAP (semitransparent, magenta). (b) Close-up view of quasi-atomic model of 70S–PDF density map featuring regions of the 50S subunit where PDF C-terminal helix (orange) is located. C-terminal helix is seen lodged between the 23SrRNA (slate) helices H24 and H47 of domains I and III, respectively, which also positions the protein helix between ribosomal proteins L22 (chocolate) and L32 (red). (c) Close-up view of quasi-atomic model of 70S–MetAP complex shows that binding location of MetAP at the tunnel exit of 50S subunit is the same as that of PDF. The ribosome-interacting loops of MetAP are seen stationed near the helix H24 of 23SrRNA (green) domain I and seems to be in direct contact with L22 (chocolate). (d) Cryo-EM map of 70S–MetAP–TF complex. MetAP density is shown in magenta, TF is in blue-green, the 30S subunit is in yellow shade, and the 50S subunit is in cyan. (e) Polypeptide exit tunnel view shows MetAP and TF density more clearly. MetAP binds to its primary binding site and is clung to the TF body. PPIase domain of TF is oriented along the line of the main body of TF. Presence of little extra density on the right side of the TF body (marked with red star) might be because of heterogeneous population of different orientation of PPIase domain of TF.

tunnel exit (Fig. 1b) attributable to MetAP. The shape of the density, representing MetAP (29 kDa), was elongated and flattened compared to the PDF density (19 kDa) and resembled the MetAP crystal structures [19,20] well in shape and size (Figs. 1d and S3b). Density corresponding to MetAP at the tunnel exit can also be detected in some of the views of the two-dimensional class averages (Fig. S2b). In contrast to the MetAP binding position proposed in a previous docking study [27], juxtaposition of PDF and MetAP bound maps (maps I and II) showed overlapping binding regions for both proteins (Fig. 2a).

Atomic model of the 70S–MetAP complex was generated in a similar way to that described before where fitting of the MetAP crystal structure was done as a rigid body. MetAP–ribosome connections were seen near the tunnel exit site on the 50S subunit, where tunnel protein L22 is located (Figs. 1d and 2c, and S3d). Unlike PDF, where a dedicated C-terminal helix exists for ribosome association, MetAP possesses several flexible loop regions over its catalytic site, likely responsible for ribosome binding (Fig. S3b). The involvement of Lys 211, Lys 218, Lys 224, and Lys 226 of MetAP (in the flexible loop regions as shown in Fig. S3b) in ribosome association has already been demonstrated [27]. Flexibility in MetAP's binding sites within the immediate vicinity was also predicted. With the positively charged loop regions, MetAP seemed to interact more profoundly with H24 (Domain III) of 23SrRNA (Fig. 2c). Thus, ribosome-binding patterns of PDF and MetAP at the tunnel exit are apparently different (Fig. 2b, c), although the binding location of the proteins is overlapping.

Globular shape and size of MetAP crystal structure match well with the density attributed to the protein. Flexible loops at the periphery (Fig. S3b, d), however, remained outside the map density, presumably due to the conformational dynamics of those regions.

The 3D map of the 70S ribosome in complex with MetAP and TF showed densities (as identified from the shapes) corresponding to both the proteins (map III, 70S–MetAP–TF complex, Figs. 2d, e, and S2c). Visualization of the stronger density corresponding to MetAP at L22–L32 location (easily visible at higher contour level) compared to the density seen in the 70S–MetAP complex (Figs. S4c and S5g, h) suggests that the presence of TF stabilizes MetAP

binding (Fig. 2d, e). Comparison of 70S–MetAP and 70S–MetAP–TF density maps confirmed the localization of primary binding site of MetAP (Fig. S4c). MetAP and TF apparently share a wide interface (Fig. S4c and S5g, h).

MetAP has multiple binding sites around the tunnel

Consistent with our observation thus far (Figs. 2a and 4a), in an earlier study conducted by Sandikci *et al*. [27], MetAP was found to compete with PDF for ribosome binding, suggesting that the primary binding site of MetAP possibly overlaps with the binding site of PDF. Nevertheless, as evident from the low ligand occupancies on the ribosome, PDF or MetAP does not exhibit robust association with the ribosome while binding individually (Fig. S5a–d). In a previously proposed model [13], however, it was suggested that there might exist a pathway where the enzymes bind simultaneously at the tunnel exit. Thus, to gain insight on the interplay between the tunnel exit-binding proteins, we further reconstructed the cryo-EM map of a complex by incubating MetAP with the 70S–PDF ribosome pre-complex (map IV, termed as 70S–PDF–MetAP complex, Figs. 3 and S2d) and found additional globular densities near the tunnel exit of 70S ribosome.

From protein shapes and sizes, the densities corresponding to PDF (~20 kDa) and MetAP (~30 kDa) could be identified (Fig. S6a, b). We found that while PDF occupied the same position as observed in the 70S–PDF complex (Fig. S4a), MetAP relocated to a position closer to L23 (Fig. 3c, d) when compared to its position on the 70S–MetAP complex (Figs. 1b and 2c). When MetAP, following PDF binding, approaches a ribosome, PDF apparently assists in MetAP binding to its secondary binding site.

Since the occupancies of the ligands are higher in this map as compared to the maps where the ligands bind individually, the ligand coordinates were fitted into the density map by keeping the unstructured regions flexible while generating the atomic model for this complex using MDFF. Atomic model of the 70S–PDF–MetAP complex demonstrated that when bound alongside PDF, MetAP almost entirely interacted with H59 (domain III of 23S rRNA) (Fig. 3d). Visualization of the stronger ligand densities (visible at higher contour level) in this complex, particularly for PDF (Figs. 3a, b, and S5e, f), suggests that the presence of MetAP in the secondary binding site (Fig. 4b) stabilizes the binding of PDF. These

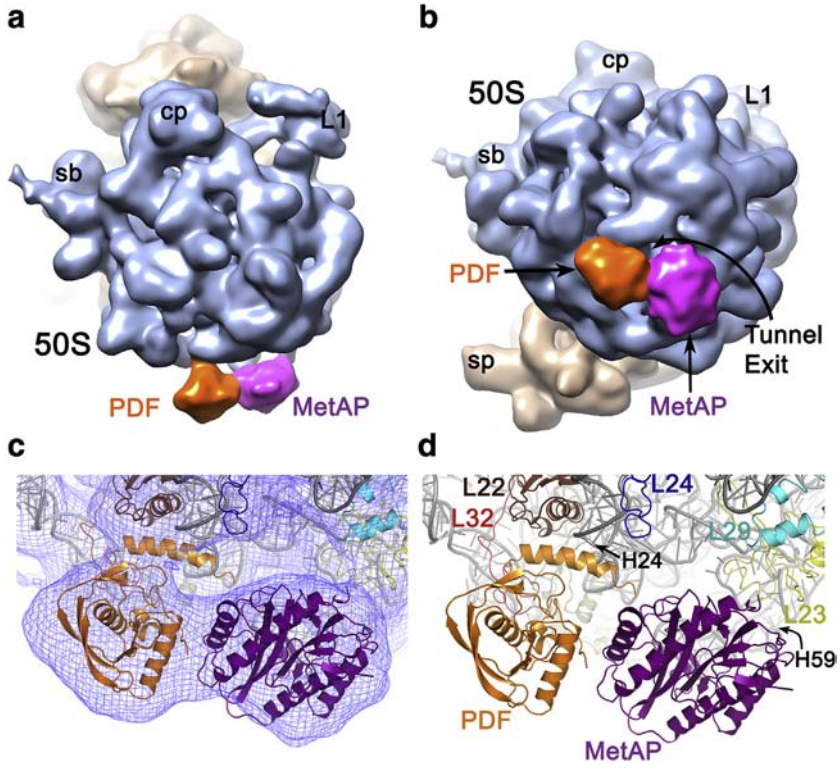

Fig. 3. Cryo-EM reconstruction of 70S ribosome–PDF–MetAP complex. (a) Cryo-EM reconstruction of *E. coli* 70S ribosome–PDF–MetAP complex, where PDF and MetAP bind together at the tunnel exit. The 30S subunit is shown in yellow, 50S subunit is in blue, and additional densities for PDF and MetAP are in orange and magenta, respectively. MetAP, unable to access its primary binding site in the presence of PDF, relocates to an adjacent region around the tunnel exit. (b) Polypeptide tunnel exit view of 50S subunit shows densities of MetAP (magenta) and PDF (orange) at the tunnel exit. (c) A close-up view of the atomic model fitted in the 70S–PDF–MetAP density map (purple blue mesh). (d) Ribosomal architecture elucidating interaction zones between PDF, MetAP, and 23S rRNA (gray), highlighting participant proteins L22 (chocolate), L32 (red), L17 (light olive), L23 (yellow), L29 (cyan), and L24 (blue), surrounding the tunnel in different colors. MetAP interacts predominantly with H59. Landmarks for 50S and 30S subunits are as in Fig. 1.

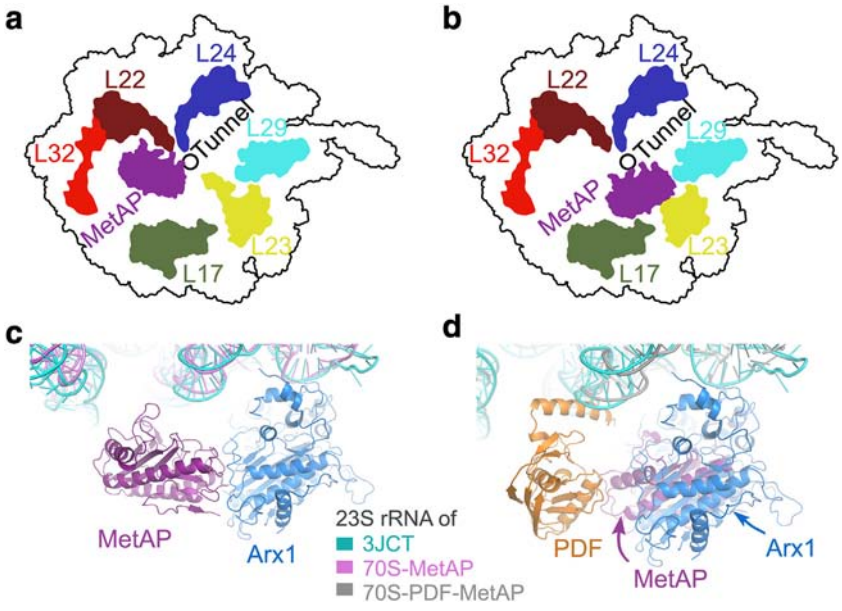

Fig. 4. Alternating binding sites for MetAP around the polypeptide tunnel exit. Illustrations of the (a) "primary binding site" of MetAP (magenta) in the absence of PDF showing MetAP's position with respect to ribosomal tunnel proteins and (b) relocation of MetAP to a neighboring location ("secondary binding site") in the presence of PDF. (c) Alignment of the fitted model of MetAP (magenta) in 70S–MetAP complex (MetAP binds at the primary binding site) and pre 60S-Arx1 model (PDB: 3JCT, blue). (d) Alignment of the fitted model of MetAP in 70S–PDF–MetAP complex (MetAP binds at the secondary binding site) and pre 60S-Arx1 model. It is clearly seen that Arx1 binding position on pre-60S yeast ribosome superposes on the secondary binding site of MetAP near the peptide exit tunnel.

observations of overlapping binding sites of PDF and MetAP (primary binding site), and alternative secondary binding site of MetAP (Fig. 4a, b) aid in understanding of some previously reported, seemingly contradictory biochemical results (see Discussion).

Notably, a eukaryotic nuclear export factor Arx1 shows structural similarity to type 2 MetAP. Cryo-EM structures of Arx1 in complex with eukaryotic ribosomal large subunit (PDB: 3JCT, 5APN, 4V7F, 6FT6) have been published. Comparison of the binding positions of Arx1 and MetAP at the tunnel exit reveals that Arx1 binding site considerably superposes on the MetAP secondary binding location (Fig. 4c, d). This observation additionally corroborates MetAP's affinity at the secondary binding location at the tunnel exit of *E. coli* 70S ribosome (Fig. 4b).

Finally, another complex was prepared by incubating 70S–PDF–MetAP pre-complex with TF (map V, Fig. S2e). In this complex, PDF was found again in the same location (Fig. S4b) and clear density corresponding to full TF was also seen (Figs. 5a, b, and S7e). Concurrent binding of TF with PDF has already been demonstrated at tunnel exit, although with a changed arrangement in TF [37]. In consistent with the observation, we found shifts in TF domains in this complex (Fig. 5c). However, the available coordinates of TF could be fully accommodated into the density attributable to TF (Fig. 5c). Although the complex was made by incubating TF with the 70S–PDF–MetAP complex, distinct density corresponding to MetAP could not be unambiguously identified in this map (map V, Fig. 5); hence, we termed this complex as 70S–PDF–TF complex. We speculate that TF, whose ribosome-binding N-terminal domain overlaps with the secondary position of MetAP, dislodged MetAP from the complex and bound ribosome instead (Fig. S4e).

Interestingly, an additional density close to L24 was found associated with the PPIase domain of TF in the 70S–PDF–TF complex (Figs. 6b and S7c). Resolution limitation of the map prohibited us to interpret this extra density. However, it may be noted here that it looked similar to the PPIase domain of TF and was strongly associated with TF density. When available TF crystal structures [28,32,39] (PDB: 3GU0, 1W26) were compared, PPIase domain was found to exhibit two distinctly different conformations where rotation of the linker domain places the PPIase domain ~90° away from one another, while other domains overlap nicely (Fig. 6a). It may be a possibility that in this complex, PPIase domain of TF coexists in two conformations (Fig. 6). A closer look at the 70S–MetAP–TF complex revealed that, although PPIase domain showed predominantly a single conformation, weak density for the other conformation was partially visible (Figs. 2e and S7b). Interaction of MetAP with TF involving larger area of contacts extended to the PPIase domain of TF presumably stabilizes one of the conformations (Figs. S5g, h, and S7a, b).

Discussion

One of the major findings of our study is the structural elucidation of MetAP relocalization in the presence of PDF. Although such relocalization of ligand is not commonly reported, similar large-scale movement of bacterial initiation factor3 (IF3) along translation initiation pathway has been identified recently [40]. It is worth mentioning again that binding site of Arx1 on pre-60S particle overlaps

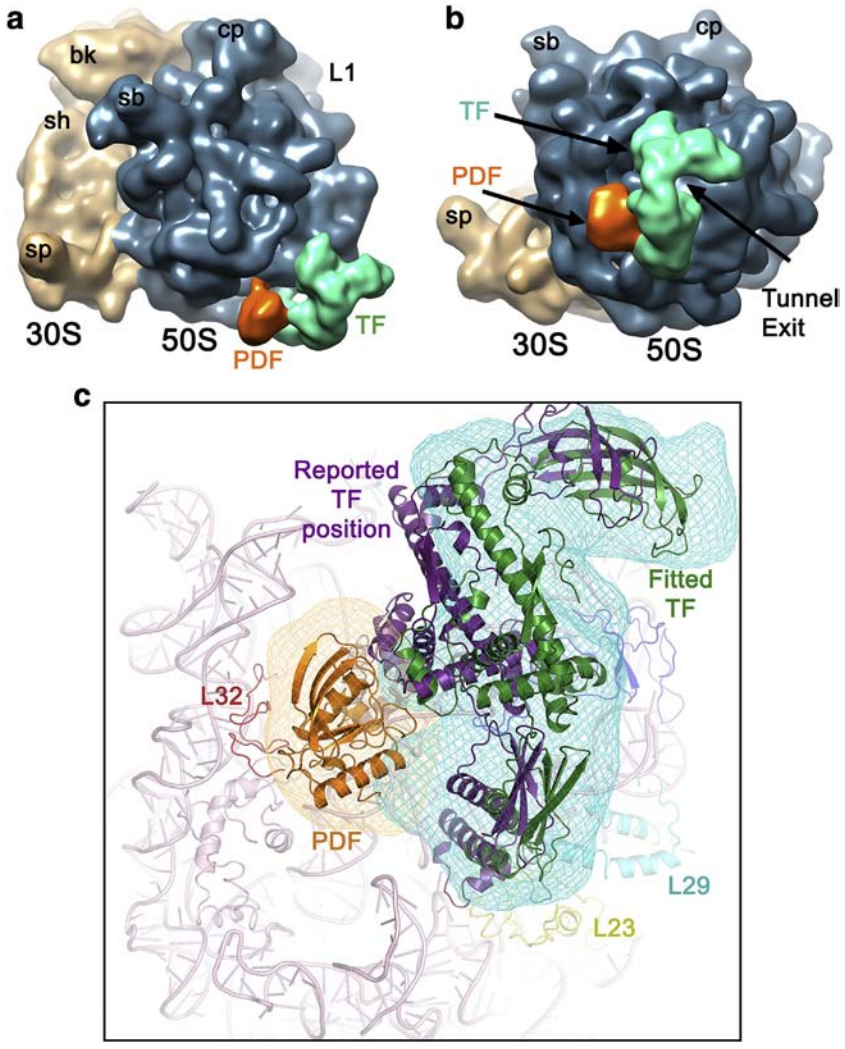

Fig. 5. Cryo-EM density map of the 70S–PDF–TF complex. (a) Cryo-EM structure of *E. coli* 70S–PDF–TF complex is shown. 30S subunit is in wheat color, 50S subunit in blue shade, PDF in orange, and TF in blue-green. (b) Tunnel view of the ribosome structure showing densities corresponding to PDF and TF full proteins near the tunnel exit. (c) Alignment of previously reported TF bound 50S subunit to the fitted coordinate of 70S–PDF–TF complex reveals direct positional clashes of TF with PDF. Shift in position of tunnel-bound TF (green) in our map from the reported TF position (violet) is seen in the presence of PDF (orange) in 70S–PDF–TF complex.

with the secondary binding site we observed for *E. coli* MetAP (type 1). It is possible that MetAPs evolved such a way in eukaryotes (eukaryotes keep both MetAP1 and MetAP2) that MetAP1 is designed to bind at the primary binding site, whereas MetAP2 is specific for the secondary binding site. It has been shown previously that MetAP competes with PDF [27], suggesting that the primary binding site of MetAP overlaps with the binding site of PDF, as we have observed when the proteins bind singly at the tunnel exit. A mechanism of action has been proposed [26], whereby PDF, MetAP, and TF bind simultaneously to the tunnel exit and where TF is responsible to guide the nascent chain to the enzymes for their respective jobs. Although concurrent binding of nascent chain processing enzymes at the tunnel exit does occur, accommodation of more than two at a time seems unlikely especially when one of the proteins is as large as TF. Based on our analyses, it is tempting to assume that PDF and MetAP may go for a sequential mode of ribosome binding at L22–L32 region to perform deformylation and methionine excision even when the tunnel is partly engaged by TF for nascent chain scanning.

Although nascent chain masked by formylation does not have any role in MetAP binding [27], MetAP may have an affinity for the unmasked nascent protein, and following the release of PDF, MetAP binds at the same location to access the deformylated nascent chain. Variability in MetAP conformation, particularly at the ribosome-binding loop regions, suggests its conformational freedom to locally scan the area for nascent chain. Besides, the structures presented here do indicate that TF likely stabilizes both PDF and MetAP when they bind singly.

A recent study showed that the association of TF and PDF with ribosome can occur simultaneously with an altered arrangement in TF [37]. The 70S–PDF–TF density map provides structural evidence that, indeed, the remarkable flexibility of TF structure [41] allows it to shift from its usual position (seen in previous TF-bound ribosome structures [28]) to accommodate itself when PDF is already present or *vice versa*. Furthermore, we found that binding of TF to the 70S–PDF–MetAP pre-

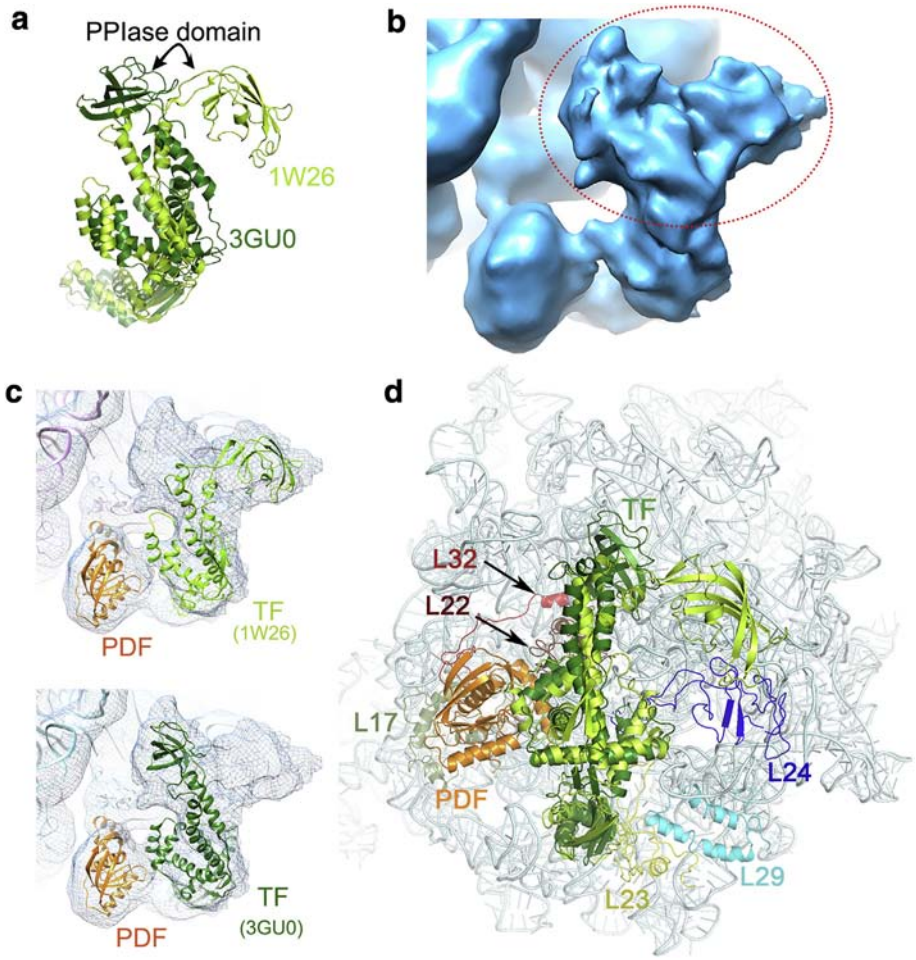

Fig. 6. Different orientations of the PPIase domain of TF. (a) Alignment of crystal structures of TF in two conformations (PDB: 3GUO and 1W26), showing large difference in orientation of the PPIase domain. (b) Bifurcated densities (circled) observed in 70S–PDF–TF reconstruction is attributed to the movement of the PPIase domain, which is known to be inherently dynamic. (c) Presence of additional PPIase domain-like density allows molecular fitting of TF (top, 1W26; bottom, 3GU0) in two conformations in the presence of PDF. (d) The model shows interactions of PDF and TF with the ribosomal counter parts. PDF binds at the same location of L22 and L32 proteins. A loop of the ribosome-binding N-terminal domain of TF interacts with L23.

complex removes MetAP to accommodate TF (likely due to steric clashes). The observation, incidentally, extrapolates to the finding of an *in vivo* study [42] showing inefficient N-formyl methionine excision in the presence of an excess TF. Although TF supposedly assists efficient binding of PDF and MetAP in sequential mode, it is possible that TF binds ribosome following complete excision of N-formyl methionine when these enzymes access ribosome simultaneously. A previous study [43] proposed binding-and-release cycles of TF–ribosome interaction that might help TF to scan for prolyl bonds in the growing polypeptide. Our results indicate a possibility of PPIase domain (catalyzes *cis*/*trans* isomerization) being captured in two different conformations in the ribosome-bound TF structures. It is tempting to propose that PPIase domain remains flexible to scan for prolyl bonds even when TF is bound to the ribosome.

However, not every nascent peptide would require TF's chaperoning assistance [44]. In such cases, simultaneous binding of PDF and MetAP may provide a time-saving route for N-formyl methionine removal. The observed delay in effective TF recruitment by RNCs [42] may thus also be explicated in light of MetAP's affinity for its secondary binding site on ribosome. Binding of PDF marks the onset of protein biogenesis. When MetAP sits next to it, they seem to mutually stabilize binding of one another. The RNA affinity of MetAP allows it to bind both sequentially and simultaneously with PDF to access the tunnel exit (Fig. 7). Moreover, a consortium of co-translational factors and chaperones over the tunnel exit site serves

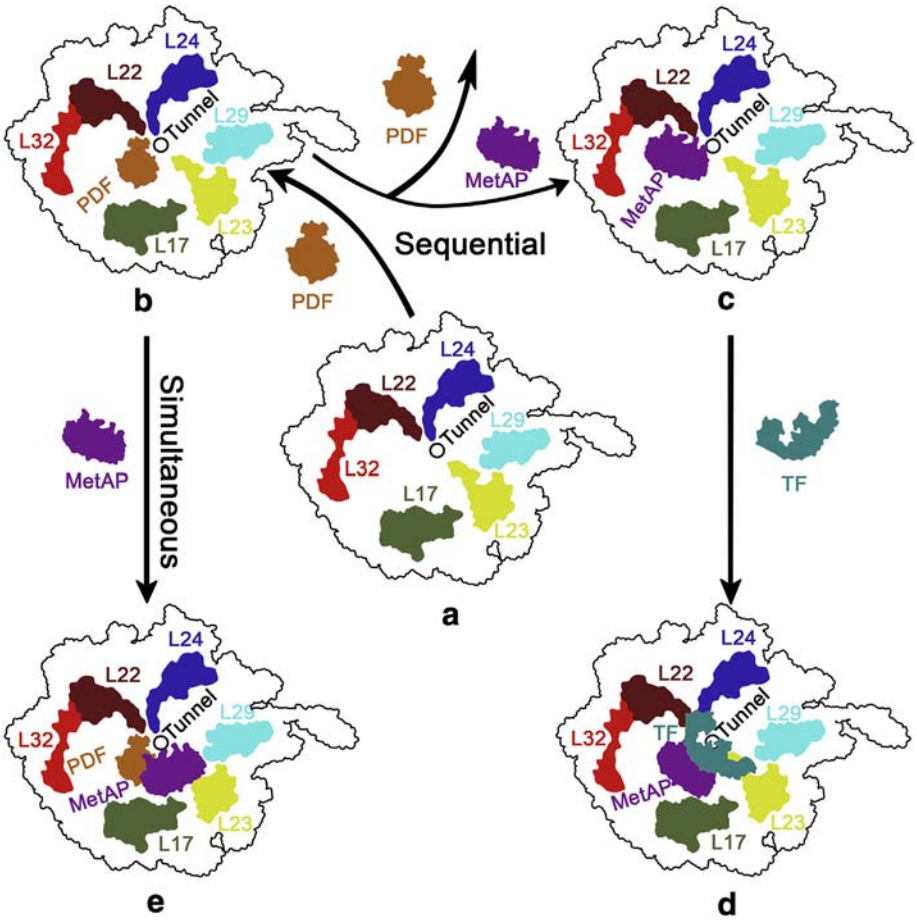

Fig. 7. Schematic representation of the proposed model for MetAP accessing alternative sites at the tunnel exit. During protein biogenesis, PDF is the first ligand to bind the 70S ribosome (a) near the tunnel exit at a specific site (b). Following the cleavage of formyl moiety from the N-terminus of the emerging nascent polypeptide chain, PDF falls off the ribosome, emptying the surface for MetAP binding (c). While in simultaneous binding mode, MetAP anchors to an adjacent region of PDF near L23, where it primarily binds to rRNA and accesses the formyl free methionine to cut it off from the nascent chain (e). For proteins that require assistance of TF chaperoning, TF can constantly guard the tunnel exit while PDF and MetAP perform their job (d).

a greater purpose and singles out a crucial role of protecting the vulnerable nascent chain at all cost.

Materials and Methods

Purification of *E. coli* 70S ribosomes

E. coli 70S ribosomes were purified following previously described protocol [45] with minor modifications. MRE 600 cells from log phase were harvested and washed thrice with buffer A [20 mM Tris–HCl (pH 7.5), 10 mM $MgOAc_2$, 100 mM NH_4Cl, 5 mM βME]. Cells were re-suspended in buffer A and lysed using French press. The lysate was centrifuged (12,000*g*, 4 °C, 20 min), supernatant was collected, and centrifugation was repeated until it stopped giving pellet. Crude ribosome was pelleted down using swing-out rotor Thermo Scientific™ AH-629 (154,000*g*, 4 °C, 2 h) from the supernatant and kept overnight in TMA10 [20 mM Tris–HCl (pH 7.5), 10 mM $MgOAc_2$, 30 mM NH_4Cl, 5 mM βME]. Pellet was re-suspended in TMA10 and homogenized for 1 h in the presence of 1 M NH_4Cl, after which the ribosomal preparation was centrifuged several times (15,000*g*, 4 °C, 20 min) until no pellet was seen. Supernatant solution was centrifuged using swing-out rotor Thermo Scientific™ AH-629 (154,000*g*, 4 °C, 2 h). The pellet was collected and kept overnight in TMA10 and then re-suspended. Sample was loaded on top of a 10%–40% linear sucrose gradient in TMA10 and centrifuged using swing-out rotor Thermo Scientific™ AH-629 (154,000*g*, 4 °C, 90 min). Gradient was collected from bottom to top and relevant fractions were pooled together. The 70S ribosome fraction was concentrated in TMA10 using 10 KD Amicon® Ultra-4 Centrifugal Filter Units (Merck Millipore) and stored at −80 °C.

Expression and purification of *E. coli* PDF

The gene encoding *E. coli* PDF was PCR amplified using primer pair: 5′ primer: 5′-CTGTTTTTGCTAGCATGTCAGTTTTGCAAGTGTTACAT-3′ and 3′ primer: 5′-GTGTCTCGAGTTAAGCCCGGGCTTTCAG-3′ and subcloned into kanamycin-resistant pET28a vector containing NheI/XhoI restriction sites (underlined) and transformed into *E. coli* BL21 (DE3). Transformed cells were grown in Luria–Bertani medium containing 0.5 mg/mL kanamycin at 37 °C until it reached an OD_{600} ~0.8. PDF expression was induced by 0.5 mM IPTG, followed by an overnight incubation of cells at 27 °C. Induced cells were harvested, washed, and lysed in PDF buffer [50 mM Hepes–KOH (pH 7.4), 100 mM NaCl, 5 mM $NiCl_2$, 1 mM TCEP, 2% glycerol]. The cell lysate was centrifuged (18,000*g*, 45 min, 4 °C), and the supernatant containing N-terminal His_6-tagged PDF was allowed to bind with nickel Sepharose resins for 3 h in the presence of 7 mM imidazole to reduce nonspecific binding. The resins were loaded onto a column and washed with PDF buffer containing 7 mM imidazole followed by 30 mM imidazole wash. The protein was then eluted with 150 mM imidazole. Imidazole was removed by exchanging with imidazole-free PDF buffer, and the protein was concentrated using Amicon® Ultra-4 Centrifugal Filter Units (Merck Millipore). The purified protein was stored at −80 °C with 20% glycerol.

Expression and purification of *E. coli* MetAP

DNA encoding MetAP, type-1a, was amplified from *E. coli* genomic DNA using the primer set: 5′ primer: 5′-TATAA G GATC C ATGGCTATCTCAATCA-3′; 3′ primer: 5′-TATAA A AGCT T TTATTCGTCGTGCGA-3′ and subcloned into pET28a vector encoding N-terminal poly-His-tag and containing BamHI/HindIII restriction sites (underlined). *E. coli* BL21 (DE3) cells were transformed with this clone and were grown to an OD_{600} of 1 at 37 °C. Cells were induced with 1 mM IPTG for 5 h at the same temperature. Cells were harvested and dissolved in +TG buffer [50 mM Hepes–NaOH (pH 8.0), 0.5 M NaCl, 10% glycerol, 0.1% Triton-X 100, and 5 mM imidazole] and lysed by sonication. The lysate was centrifuged (18,000*g*, 4 °C, 20 min), and the soluble fraction was filtered through 0.22 µm pore size sterile filter. The filtered soluble fraction was loaded on top of the +TG pre-equilibrated Ni^{+2}-NTA affinity flow column, and the column was washed with the same buffer, followed by −TG buffer [50 mM Hepes–NaOH, (pH 8.0), 0.5 M NaCl, and 5 mM imidazole]. The protein was eluted with elution buffer [50 mM Hepes (pH 8.0), 0.5 M NaCl, and 150 mM imidazole] and then buffer exchanged in storage buffer [50 mM Hepes (pH 8.0), 150 mM NaCl] and concentrated using 10 KD Amicon® Ultra-4 Centrifugal Filter Units (Merck Millipore). All the buffer compositions were made following standard protocol [17].

Expression and purification of *E. coli* TF

BL21 (DE3) cells were transformed with pET28a vector containing the gene encoding *E. coli* TF. Transformed cells were grown in Luria–Bertani medium at 37 °C until it reached an OD_{600} ~0.8. Cells were induced with 0.4 mM IPTG at 37 °C for 4 h. Cells were harvested, washed, and dissolved in lysis buffer [50 mM phosphate buffer (pH 8), 500 mM NaCl, 1 mM PMSF, 10 mM imidazole] and then lysed and centrifuged (18,000*g*, 4 °C, 45 min). The supernatant was collected and allowed to bind to Ni Sepharose resin for an hour. The protein-bound resin was washed repeatedly with lysis buffer. His_6 tagged TF was then eluted at 250 mM imidazole concentration, concentrated using 10 KD Amicon® Ultra-4 Centrifugal Filter Units (Merck Millipore) in storage buffer [20 mM Tris–HCl (pH 7.5), 100 mM NaCl, 1 mM TCEP] and stored at −80 °C with 20% glycerol.

Gel electrophoresis and Western blot analysis

Ribosome samples with or without bound proteins were loaded on a 12% denaturing SDS-PAGE gel and stained with Coomassie blue for visualizing protein bands. Recombinant proteins PDF, MetAP, and TF were localized and estimated to have molecular weights of 20, 30, and 55 kDa, respectively.

Western blot analysis was performed for ribosomes with or without the bound recombinant protein His_6-tagged PDF. Blots were probed with anti-His antibody (obtained from GCC Biotech, India). Binding of the secondary HRP-conjugated anti-rabbit antibodies (Millipore, USA) was analyzed using ImmunoCruz (Santa Cruz Biotechnology Inc., USA).

Mass spectrometry analysis

Mass analysis was performed using 4800 MALDI TOF/TOF (model 4800; Applied Biosystems, USA) instrument operated in “reflectron” mode. For MS/MS analysis, protein bands were excised from the gel and digested in gel using In-Gel Tryptic Digestion Kit (Thermo Scientific™). Mass analysis was performed using a saturated solution of CHCA (α-cyano-4-hydroxycinnamic acid) in 50% acetonitrile/0.1% trifluoroacetic acid. The MS/MS peaks of the most intense mass ions were searched against the NCBInr Database using MASCOT software (Matrix Science Ltd., London, UK). Peptides were matched to proteins when statistically significant MASCOT probability scores (<0.05) were consistent with experimental MW of the protein.

Ribosome co-sedimentation assay

Ribosomes (0.24 μM) were incubated with a 60-fold excess of recombinant proteins (14.4 μM) for 30 min at 37 °C in binding buffers [20 mM Hepes–KOH (pH 7.5), 100 mM NH_4OAc, 20 mM $MgCl_2$, and 1 mM TCEP] and [20 mM Hepes (pH 7.5), 50 mM KOAc, 15 mM $Mg(OAc)_2$, 0.1 mM $CoCl_2$] for PDF/TF and MetAP, respectively. Samples were pelleted through 5% sucrose cushion using fixed angle Thermo Scientific™ T-890 rotor (173,000*g*, 4 °C, 7 h) and the supernatants and pellets were separately collected. Pellets were re-suspended, and the supernatants were buffer exchanged in binding buffer and concentrated using 10 KD Amicon® Ultra-4 Centrifugal Filter Units (Merck Millipore). The final volumes of dissolved pellet and concentrated supernatants were kept the same. Both were then resolved in a 12% SDS-PAGE gel. The absence of protein bands in the control lanes indicates that co-sedimentation of a protein occurs only due to the specific interaction of a protein with the ribosome. The binding of proteins was further validated by MS/MS and was Western blotted in the case of PDF, since ribosomal proteins S4 and L4 were also of similar molecular weights as recombinant PDF.

Sample preparation for cryo-EM imaging

For preparation of complexes, all ligand concentrations were kept at 30 to 60 fold higher than 70S ribosomes during incubations to keep the ligand bound 70S population high.

Co-sedimentation [27] pellet of the 70S–PDF complex was dissolved in PDF binding buffer. Thirty-fold excess PDF (9 μM) was added and incubated with the complex at 37 °C for 30 min under constant shaking condition and then kept on ice until grid preparation.

Sixty-fold excess purified MetAP (48 μM) was incubated with co-sedimented 70S–MetAP complex (70S concentration 0.8 μM) in MetAP binding buffer [20 mM Hepes (pH 7.5), 50 mM KOAc, 15 mM $Mg(OAc)_2$, 0.1 mM $CoCl_2$] at 37 °C for 10 min under shaking condition and then incubated on ice until grid preparation.

70S–MetAP pre-complex (70S concentration 0.4 μM) was incubated with 30-fold excess TF (12 μM) at 37 °C for 20 min in binding buffer to get 70S–MetAP–TF complex.

To prepare the 70S–PDF–MetAP complex, 70S ribosome (70S concentration 0.6 μM) was incubated first with PDF in PDF binding buffer (37 °C, 30 min, with shaking), and activated MetAP was then added to the reaction mixture and incubated at 37 °C for 10 min. The reaction mixture was kept on ice until grid preparation.

For preparation of the 70S–PDF–TF complex, 70S ribosome (0.55 μM) was incubated with 60-fold excess PDF (33 μM) in binding buffer, followed by activated MetAP and then with TF.

MetAP is activated by incubating it in MetAP binding buffer at Co^{2+} concentration 0.05 mM.

Cryo-grids of the 70S–protein complexes were prepared following standard procedures using Vitrobot Mark IV (FEI) [46]. Tedpella Lacey grids were used for 70S–PDF complexes with a blotting time of 6.5 s. For all other complexes, Tedpella Quantifoil grids were used with blotting time of 7 s.

Cryo-EM and 3D image processing

Data were collected using 4K × 4K Charged Coupled Device (CCD) camera with a physical pixel size of 15 μm (corresponding to a pixel size of 1.89 Å/pixel on the object scale) on an FEI (Eindhoven, the Netherlands) Tecnai 300 kV G2 polara field emission gun electron microscope, equipped with low-dose kit and cryo-transfer holder at a total magnification of 78,894×. Low-dose mode (~$10e^-/Å^2$) was used during imaging.

Data were primarily processed with SPIDER [47,48] package (Version: 23.02) where gold standard protocol [49,50] has recently been incorporated. Power spectrum and CTF (Contrast Transfer Function) of each micrograph were calculated by CTFFIND4 [51]. Micrographs (~200–400 for each data set) with defocus value in the range of 1 to 4 μm were checked for drift and astigmatism. Selected micrographs were CTF corrected by phase flipping, and the phase-flipped micrographs were used for particle windowing. Particles were selected based on a fast locally normalized correlation algorithm [52,53] using a blank 70S ribosome. Projections of the blank 70S ribosome, filtered at ~30Å resolution and with desired dimension and pixel size (as a reference 3D map) at uniform Euler angles, were used to find different orientations of particle images. Aligned particles were classified by subjecting them to multivariate data analysis and K-means classification and were screened class-wise to make up a clean data set [54–57]. Total numbers of particles after verification were as follows: ~44,000 for 70S–PDF complex, ~35,000 for 70S–MetAP complex, ~19,500 for 70S–MetAP–TF complex, ~35,000 for 70S–PDF–MetAP complex, and ~20,900 for 70S–PDF–TF complex. Refinement of the initial 3D volume was done by dividing the data set in two halves following the newly developed gold standard protocol [49] and by iteratively adjusting the angles for finer resolution. Back projection, conjugate gradients with regularization (implemented in SPIDER by "BP CG" command), was used for generating 3D volume during refinement. Fourier amplitudes of 3D volumes were enhanced using the x-ray scattering data [58]. To present the figures, the 30S and 50S subunits and protein densities were isolated from the amplitude-enhanced maps following the standard protocol of difference mapping in SPIDER (https://spider.wadsworth.org/spider_doc/spider/docs/techs/diffmaps/isolate.html) or segmentation protocol

implemented in Chimera [59]. Pymol (DeLano Scientific) and Chimera were used for cryo-EM map analysis and preparation of illustrations. ResMap [60] was used for calculation of local resolution of the maps. Xmipp [61] image conversion program was used for conversion of micrographs from one format to another. EMDB Fourier Shell Correlation (FSC) server was used to show the FSC plots (https://www.ebi.ac.uk/pdbe/emdb/validation/fsc/).

Molecular modeling

Atomic models of each map were independently generated using MDFF [62]. We have followed the procedure described by Trabuco *et al*. [63]. Briefly, initial rigid body fittings were done by Chimera or Pymol. The rRNA coordinates (PDBs: 30S, 2I2U; 50S, 2I2V) were flexibly fitted into the density maps first. Then, keeping the rRNA coordinates rigid, the tunnel bound ribosomal protein coordinates were fitted. Finally, the ribosomal protein and rRNA coordinates were kept rigid, and the ligand coordinates were fitted. Due to low occupancies of the ligands in maps of 70S–PDF and 70S–MetAP complexes, the ligands were fitted as rigid bodies in those maps. In the other three maps, PDF and MetAP coordinates were fitted as rigid bodies where only the unstructured loop regions were kept flexible. Each of the TF domains was allowed to be fitted as rigid body keeping the unstructured linkers (connecting the domains) flexible. VMD [64] and NAMD [65] were used for flexible fitting of crystal structure co-ordinates into the cryo-EM density maps. The fitted models of PDF in density maps of 70S–PDF, 70S–PDF–TF and 70S–PDF–MetAP complexes were compared and found almost identical. The positions of MetAP models in 70S–MetAP and 70S–MetAP–TF maps were also found to be similar. However, due to low ligand occupancy, the orientation of MetAP model in 70S–MetAP map may not be very accurate.

Accession numbers

Deposition of the cryo-EM density maps and coordinates in the Electron Microscopy Data Bank (EMDB) and RCSB data bank has been done. The accession numbers of the maps are EMD-9750, EMD-9752, EMD-9753, EMD-9759, and EMD-9778, and related fitted coordinates of the ligands are 6IY7, 6IZ7, 6IZI, 6J0A, and 6J45, respectively.

CRediT authorship contribution statement

Sayan Bhakta: Data curation, Formal analysis, Investigation, Methodology, Writing - original draft, Writing - review & editing. **Shirin Akbar:** Data curation, Formal analysis, Investigation, Methodology, Writing - original draft, Writing - review & editing. **Jayati Sengupta:** Conceptualization, Data curation, Formal analysis, Funding acquisition, Investigation, Methodology, Project administration, Resources, Supervision, Writing - original draft, Writing - review & editing.

Acknowledgments

This work was primarily supported by Science and Engineering Research Board (SERB), India, sponsored project (grant ID: SB/SO/BB-0025/2014), and CSIR-Indian Institute of Chemical Biology, Kolkata, India. We sincerely thank Prof. Marin van Heel and Dr. Ilic Zoran (Wadsworth Center, NY, USA) for critically checking the manuscript. We greatly appreciate the help from Central Instrumentation Facilities (CIF) of the CSIR Indian Institute of Chemical biology. We acknowledge the supercomputing facility provided by CSIR Fourth Paradigm Institute (http://www.cmmacs.ernet.in). We sincerely thank Mr. Chiranjit Biswas for cryo-grid preparation and collection of cryo-EM images of five ribosomal complexes; Dr. Chandana Barat, St. Xavier's College, Kolkata, for providing TF clone; and Ms. Thokala Ravali and Mr. Soumya Basak for assisting in preliminary cryo-EM data processing. Fund provided by NIPER for project students is gratefully acknowledged. S.B. and S.A. acknowledge CSIR, India, for senior research fellowship.

Appendix A. Supplementary data

Supplementary data to this article can be found online at https://doi.org/10.1016/j.jmb.2019.02.002.

Received 17 September 2018;
Received in revised form 1 February 2019;
Accepted 1 February 2019
Available online 10 February 2019

Keywords:
E. coli 70S ribosome;
peptide deformylase;
methionine aminopeptidase;
trigger factor;
nascent chain processing

†Equal contribution.

Abbreviations used:
PDF, peptide deformylase; MetAP, methionine aminopeptidase; TF, trigger factor; SRP, signal recognition particle; rRNA, ribosomal RNA; r-proteins, ribosomal proteins; L-proteins, large subunit proteins; RNC, ribosome-nascent-chain complex; PPIase, peptidylprolyl transferase; cryo-EM, cryo-electron microscopy; MDFF, molecular dynamics flexible fitting.

References

[1] G. Kramer, D. Boehringer, N. Ban, B. Bukau, The ribosome as a platform for co-translational processing, folding and targeting of newly synthesized proteins, Nat. Struct. Mol. Biol. 16 (2009) 589–597.

[2] C.V. Robinson, A. Sali, W. Baumeister, The molecular sociology of the cell, Nature 450 (2007) 973–982.

[3] V. Berk, W. Zhang, R.D. Pai, J.H. Cate, Structural basis for mRNA and tRNA positioning on the ribosome, Proc. Natl. Acad. Sci. U. S. A. 103 (2006) 15830–15834.

[4] A. Breiman, S. Fieulaine, T. Meinnel, C. Giglione, The intriguing realm of protein biogenesis: facing the green co-translational protein maturation networks, Biochim. Biophys. Acta 1864 (2016) 531–550.

[5] C. Schaffitzel, M. Oswald, I. Berger, T. Ishikawa, J.P. Abrahams, H.K. Koerten, R.I. Koning, N. Ban, Structure of the *E. coli* signal recognition particle bound to a translating ribosome, Nature 444 (2006) 503–506.

[6] M. Halic, T. Becker, M.R. Pool, C.M. Spahn, R.A. Grassucci, J. Frank, R. Beckmann, Structure of the signal recognition particle interacting with the elongation-arrested ribosome, Nature 427 (2004) 808–814.

[7] M. Halic, M. Blau, T. Becker, T. Mielke, M.R. Pool, K. Wild, I. Sinning, R. Beckmann, Following the signal sequence from ribosomal tunnel exit to signal recognition particle, Nature 444 (2006) 507–511.

[8] L.F. Estrozi, D. Boehringer, S.O. Shan, N. Ban, C. Schaffitzel, Cryo-EM structure of the *E. coli* translating ribosome in complex with SRP and its receptor, Nat. Struct. Mol. Biol. 18 (2011) 88–90.

[9] T. Meinnel, Y. Mechulam, S. Blanquet, Methionine as translation start signal: a review of the enzymes of the pathway in *Escherichia coli*, Biochimie 75 (1993) 1061–1075.

[10] C. Giglione, S. Fieulaine, T. Meinnel, N-terminal protein modifications: bringing back into play the ribosome, Biochimie 114 (2015) 134–146.

[11] S. Ragusa, S. Blanquet, T. Meinnel, Control of peptide deformylase activity by metal cations, J. Mol. Biol. 280 (1998) 515–523.

[12] P.T. Rajagopalan, A. Datta, D. Pei, Purification, characterization, and inhibition of peptide deformylase from *Escherichia coli*, Biochemistry 36 (1997) 13910–13918.

[13] R. Bingel-Erlenmeyer, R. Kohler, G. Kramer, A. Sandikci, S. Antolic, T. Maier, C. Schaffitzel, B. Wiedmann, B. Bukau, N. Ban, A peptide deformylase-ribosome complex reveals mechanism of nascent chain processing, Nature 452 (2008) 108–111.

[14] J. Solbiati, A. Chapman-Smith, J.L. Miller, C.G. Miller, J.E. Cronan Jr., Processing of the N termini of nascent polypeptide chains requires deformylation prior to methionine removal, J. Mol. Biol. 290 (1999) 607–614.

[15] F. Frottin, A. Martinez, P. Peynot, S. Mitra, R.C. Holz, C. Giglione, T. Meinnel, The proteomics of N-terminal methionine cleavage, Mol. Cell. Proteomics 5 (2006) 2336–2349.

[16] X.V. Hu, X. Chen, K.C. Han, A.S. Mildvan, J.O. Liu, Kinetic and mutational studies of the number of interacting divalent cations required by bacterial and human methionine aminopeptidases, Biochemistry 46 (2007) 12833–12843.

[17] A. Addlagatta, M.L. Quillin, O. Omotoso, J.O. Liu, B.W. Matthews, Identification of an SH3-binding motif in a new class of methionine aminopeptidases from *Mycobacterium tuberculosis* suggests a mode of interaction with the ribosome, Biochemistry 44 (2005) 7166–7174.

[18] W.T. Lowther, B.W. Matthews, Metalloaminopeptidases: common functional themes in disparate structural surroundings, Chem. Rev. 102 (2002) 4581–4608.

[19] W.T. Lowther, A.M. Orville, D.T. Madden, S. Lim, D.H. Rich, B.W. Matthews, *Escherichia coli* methionine aminopeptidase: implications of crystallographic analyses of the native, mutant, and inhibited enzymes for the mechanism of catalysis, Biochemistry 38 (1999) 7678–7688.

[20] W.T. Lowther, Y. Zhang, P.B. Sampson, J.F. Honek, B.W. Matthews, Insights into the mechanism of *Escherichia coli* methionine aminopeptidase from the structural analysis of reaction products and phosphorus-based transition-state analogues, Biochemistry 38 (1999) 14810–14819.

[21] M.M. Elvekrog, P. Walter, Dynamics of co-translational protein targeting, Curr. Opin. Chem. Biol. 29 (2015) 79–86.

[22] A. Jomaa, Y.H. Fu, D. Boehringer, M. Leibundgut, S.O. Shan, N. Ban, Structure of the quaternary complex between SRP, SR, and translocon bound to the translating ribosome, Nat. Commun. 8 (2017), 15470.

[23] I. Saraogi, S.O. Shan, Molecular mechanism of co-translational protein targeting by the signal recognition particle, Traffic 12 (2011) 535–542.

[24] Q.A. Valent, D.A. Kendall, S. High, R. Kusters, B. Oudega, J. Luirink, Early events in preprotein recognition in *E. coli*: interaction of SRP and trigger factor with nascent polypeptides, EMBO J. 14 (1995) 5494–5505.

[25] S.C. Ogg, P. Walter, SRP samples nascent chains for the presence of signal sequences by interacting with ribosomes at a discrete step during translation elongation, Cell 81 (1995) 1075–1084.

[26] C. Giglione, S. Fieulaine, T. Meinnel, Cotranslational processing mechanisms: towards a dynamic 3D model, Trends Biochem. Sci. 34 (2009) 417–426.

[27] A. Sandikci, F. Gloge, M. Martinez, M.P. Mayer, R. Wade, B. Bukau, G. Kramer, Dynamic enzyme docking to the ribosome coordinates N-terminal processing with polypeptide folding, Nat. Struct. Mol. Biol. 20 (2013) 843–850.

[28] L. Ferbitz, T. Maier, H. Patzelt, B. Bukau, E. Deuerling, N. Ban, Trigger factor in complex with the ribosome forms a molecular cradle for nascent proteins, Nature 431 (2004) 590–596.

[29] D. Baram, E. Pyetan, A. Sittner, T. Auerbach-Nevo, A. Bashan, A. Yonath, Structure of trigger factor binding domain in biologically homologous complex with eubacterial ribosome reveals its chaperone action, Proc. Natl. Acad. Sci. U. S. A. 102 (2005) 12017–12022.

[30] A. Hoffmann, B. Bukau, G. Kramer, Structure and function of the molecular chaperone trigger factor, Biochim. Biophys. Acta 1803 (2010) 650–661.

[31] A. Hoffmann, A.H. Becker, B. Zachmann-Brand, E. Deuerling, B. Bukau, G. Kramer, Concerted action of the ribosome and the associated chaperone trigger factor confines nascent polypeptide folding, Mol. Cell 48 (2012) 63–74.

[32] E. Martinez-Hackert, W.A. Hendrickson, Promiscuous substrate recognition in folding and assembly activities of the trigger factor chaperone, Cell 138 (2009) 923–934.

[33] G. Kramer, T. Rauch, W. Rist, S. Vorderwulbecke, H. Patzelt, A. Schulze-Specking, N. Ban, E. Deuerling, B. Bukau, L23 protein functions as a chaperone docking site on the ribosome, Nature 419 (2002) 171–174.

[34] B.J. Greber, D. Boehringer, C. Montellese, N. Ban, Cryo-EM structures of Arx1 and maturation factors Rei1 and Jjj1 bound to the 60S ribosomal subunit, Nat. Struct. Mol. Biol. 19 (2012) 1228–1233.

[35] C. Leidig, M. Thoms, I. Holdermann, B. Bradatsch, O. Berninghausen, G. Bange, I. Sinning, E. Hurt, R. Beckmann, 60S ribosome biogenesis requires rotation of the 5S ribonucleoprotein particle, Nat. Commun. 5 (2014) 3491.
[36] S. Wu, B. Tutuncuoglu, K. Yan, H. Brown, Y. Zhang, D. Tan, M. Gamalinda, Y. Yuan, Z. Li, J. Jakovljevic, C. Ma, J. Lei, M. Q. Dong, J.L. Woolford Jr., N. Gao, Diverse roles of assembly factors revealed by structures of late nuclear pre-60S ribosomes, Nature 534 (2016) 133–137.
[37] T. Bornemann, W. Holtkamp, W. Wintermeyer, Interplay between trigger factor and other protein biogenesis factors on the ribosome, Nat. Commun. 5 (2014) 4180.
[38] A. Becker, I. Schlichting, W. Kabsch, D. Groche, S. Schultz, A.F. Wagner, Iron center, substrate recognition and mechanism of peptide deformylase, Nat. Struct. Biol. 5 (1998) 1053–1058.
[39] F. Merz, D. Boehringer, C. Schaffitzel, S. Preissler, A. Hoffmann, T. Maier, A. Rutkowska, J. Lozza, N. Ban, B. Bukau, E. Deuerling, Molecular mechanism and structure of trigger factor bound to the translating ribosome, EMBO J. 27 (2008) 1622–1632.
[40] T. Hussain, J.L. Llacer, B.T. Wimberly, J.S. Kieft, V. Ramakrishnan, Large-scale movements of IF3 and tRNA during bacterial translation initiation, Cell 167 (2016) 133–144 e13.
[41] T. Saio, X. Guan, P. Rossi, A. Economou, C.G. Kalodimos, Structural basis for protein antiaggregation activity of the trigger factor chaperone, Science 344 (2014) 1250494.
[42] E. Oh, A.H. Becker, A. Sandikci, D. Huber, R. Chaba, F. Gloge, R.J. Nichols, A. Typas, C.A. Gross, G. Kramer, J.S. Weissman, B. Bukau, Selective ribosome profiling reveals the cotranslational chaperone action of trigger factor in vivo, Cell 147 (2011) 1295–1308.
[43] R. Maier, B. Eckert, C. Scholz, H. Lilie, F.X. Schmid, Interaction of trigger factor with the ribosome, J. Mol. Biol. 326 (2003) 585–592.
[44] C.B. Anfinsen, Principles that govern the folding of protein chains, Science 181 (1973) 223–230.
[45] B. Das, S. Chattopadhyay, A.K. Bera, C. Dasgupta, In vitro protein folding by ribosomes from *Escherichia coli*, wheat germ and rat liver: the role of the 50S particle and its 23S rRNA, Eur. J. Biochem. 235 (1996) 613–621.
[46] R.A. Grassucci, D.J. Taylor, J. Frank, Preparation of macromolecular complexes for cryo-electron microscopy, Nat. Protoc. 2 (2007) 3239–3246.
[47] J. Frank, M. Radermacher, P. Penczek, J. Zhu, Y. Li, M. Ladjadj, A. Leith, SPIDER and WEB: processing and visualization of images in 3D electron microscopy and related fields, J. Struct. Biol. 116 (1996) 190–199.
[48] T.R. Shaikh, H. Gao, W.T. Baxter, F.J. Asturias, N. Boisset, A. Leith, J. Frank, SPIDER image processing for single-particle reconstruction of biological macromolecules from electron micrographs, Nat. Protoc. 3 (2008) 1941–1974.
[49] R. Henderson, A. Sali, M.L. Baker, B. Carragher, B. Devkota, K.H. Downing, E.H. Egelman, Z. Feng, J. Frank, N. Grigorieff, W. Jiang, S.J. Ludtke, O. Medalia, P.A. Penczek, P.B. Rosenthal, M.G. Rossmann, M.F. Schmid, G.F. Schroder, A.C. Steven, D.L. Stokes, J.D. Westbrook, W. Wriggers, H. Yang, J. Young, H.M. Berman, W. Chiu, G.J. Kleywegt, C.L. Lawson, Outcome of the first electron microscopy validation task force meeting, Structure 20 (2012) 205–214.
[50] A. AEvarsson, E. Brazhnikov, M. Garber, J. Zheltonosova, Y. Chirgadze, S. al-Karadaghi, L.A. Svensson, A. Liljas, Three-dimensional structure of the ribosomal translocase: elongation factor G from *Thermus thermophilus*, EMBO J. 13 (1994) 3669–3677.
[51] A. Rohou, N. Grigorieff, CTFFIND4: fast and accurate defocus estimation from electron micrographs, J. Struct. Biol. 192 (2015) 216–221.
[52] B.K. Rath, J. Frank, Fast automatic particle picking from cryo-electron micrographs using a locally normalized cross-correlation function: a case study, J. Struct. Biol. 145 (2004) 84–90.
[53] A.M. Roseman, Particle finding in electron micrographs using a fast local correlation algorithm, Ultramicroscopy 94 (2003) 225–236.
[54] M. van Heel, Comments on: 'Classification of images of biomolecular assemblies: a study of ribosomes and ribosomal subunits of *Escherichia coli*', J. Microsc. 159 (1990) 113–117.
[55] M. van Heel, Multivariate statistical classification of noisy images (randomly oriented biological macromolecules), Ultramicroscopy 13 (1984) 165–183.
[56] M. van Heel, J. Frank, Use of multivariate statistics in analysing the images of biological macromolecules, Ultramicroscopy 6 (1981) 187–194.
[57] M. Schatz, M. van Heel, Invariant classification of molecular views in electron micrographs, Ultramicroscopy 32 (1990) 255–264.
[58] I.S. Gabashvili, R.K. Agrawal, C.M. Spahn, R.A. Grassucci, D.I. Svergun, J. Frank, P. Penczek, Solution structure of the *E. coli* 70S ribosome at 11.5 Å resolution, Cell 100 (2000) 537–549.
[59] E.F. Pettersen, T.D. Goddard, C.C. Huang, G.S. Couch, D.M. Greenblatt, E.C. Meng, T.E. Ferrin, UCSF Chimera—a visualization system for exploratory research and analysis, J. Comput. Chem. 25 (2004) 1605–1612.
[60] J. Zhao, J. Wang, D.J. Chen, S.R. Peterson, J. Trewhella, The solution structure of the DNA double-stranded break repair protein Ku and its complex with DNA: a neutron contrast variation study, Biochemistry 38 (1999) 2152–2159.
[61] R. Marabini, I.M. Masegosa, M.C. San Martin, S. Marco, J.J. Fernandez, L.G. de la Fraga, C. Vaquerizo, J.M. Carazo, Xmipp: an image processing package for electron microscopy, J. Struct. Biol. 116 (1996) 237–240.
[62] L.G. Trabuco, E. Villa, E. Schreiner, C.B. Harrison, K. Schulten, Molecular dynamics flexible fitting: a practical guide to combine cryo-electron microscopy and x-ray crystallography, Methods 49 (2009) 174–180.
[63] L.G. Trabuco, E. Villa, K. Mitra, J. Frank, K. Schulten, Flexible fitting of atomic structures into electron microscopy maps using molecular dynamics, Structure 16 (2008) 673–683.
[64] W. Humphrey, A. Dalke, K. Schulten, VMD: visual molecular dynamics, J. Mol. Graph. 14 (1996) 33–38 (27–8).
[65] J.C. Phillips, R. Braun, W. Wang, J. Gumbart, E. Tajkhorshid, E. Villa, C. Chipot, R.D. Skeel, L. Kale, K. Schulten, Scalable molecular dynamics with NAMD, J. Comput. Chem. 26 (2005) 1781–1802.